LRP 687/00 December 2000

Global linear gyrokinetic simulations in quasi-symmetric configurations

G. Jost, T.M. Tran, W.A. Cooper,
L. Villard, K. Appert

Submitted for publication in
Physics of Plasmas

ISSN 0458-5895

Global Linear Gyrokinetic Simulations in Quasi-Symmetric Configurations

G. Jost, T. M. Tran, W. A. Cooper, L. Villard, K. Appert

Centre de Recherches en Physique des Plasmas, Association Euratom - Confédération Suisse

Ecole Polytechnique Fédérale de Lausanne, PPB - CH-1015 Ecublens/Switzerland

(November 28, 2000)

Abstract

We present the first global linear study of electrostatic drift waves in two realistic quasi-symmetric configurations, namely the Quasi-Axially symmetric Stellarator with three fields periods (QAS3) and the Helically Symmetric eXperiment (HSX). Effects of the shape of the plasma on the growth rate and frequency of the Ion Temperature Gradient driven mode are investigated by varying the quasi-symmetric configurations to an equivalent symmetric system. The calculations have been performed with the 3D global gyrokinetic code EUTERPE in the magnetic configurations provided by the MHD equilibrium code VMEC. We assume gyrokinetic ions and adiabatic electrons. In QAS3, results show that the drift waves are mainly affected by the global magnetic shear and barely by the shape of the plasma or the local magnetic shear. They are then very close to those obtained for a tokamak. On the other hand, results for the HSX configuration, show a clear 3D effect, namely a strong toroidal variation of the drift wave mode structure. This variation is a clear structure of the 3D plasma shape. However, first results show that the growth rate of the ITG driven mode is largely unaffected by this effect.

52.35.Kt, 52.55.Hc, 52.65Tt

I. INTRODUCTION

It is now commonly accepted that the turbulence resulting from the nonlinear saturation of microinstabilities, particularly Ion Temperature Gradient (ITG) driven modes, plays an important role in the anomalous transport observed in tokamaks [1,2]. Theoretically and experimentally, they have been studied intensively for axisymmetric magnetic configurations (tokamaks), whereas for other configurations (2D systems with helical symmetry, full 3D systems) the neoclassical theory has been the main focus of transport studies. In a plasma characterized by an averaged plasma pressure $\langle p \rangle$ much smaller than the averaged magnetic pressure $\langle B^2 \rangle$, drift waves are essentially ion acoustic waves destabilized by the inhomogeneities of the plasma [3]. They are characterized by a low frequency, $\omega < 1\text{MHz} \ll \Omega$, and a long parallel wavelength $\omega/k_{||} \gg v_{thi}$; the ion cyclotron frequency is $\Omega \approx 100$ MHz in a typical fusion reactor and only long parallel wavelengths can avoid strong ion Landau damping due to wave-ion interaction. Here, v_{thi} and $k_{||}$ denote the thermal velocity of the ions and the parallel component to the magnetic field of the wave vector $\vec{k}$, respectively.

The lack of symmetry is the main problem of a full 3D configuration, small neoclassical transport and confinement of α particles, which are a minimum requirement for a reactor, are very difficult to achieve. In order to recover the good neoclassical confinement properties of symmetric configurations, quasi-symmetric (QS) systems have been proposed [4]. Several projects based on this principle are currently developed, for example the Helically Symmetric eXperiment (HSX) at the University of Wisconsin [5] and the National Compact Stellarator eXperiment (NCSX) [6] a quasi-axisymmetric stellarator at the Princeton Plasma Physics Laboratory. While good neoclassical properties are expected within the next generation of stellarators, the currently operating devices are characterized by a strong neoclassical transport. However, in contrast with tokamaks, there is no experimental evidence of anomalous transport in the plasma core in these devices. Transport in stellarators is currently well explained with the help of the neoclassical theory except near the edge of the configurations where turbulence occurs [9]. This explains the small number of theoretical studies on

anomalous transport in these devices [10–16]. As the stellarator experiments become larger and more expensive the theory ought to prepare interpretation tools even if, in the best case, they will not be needed. Since the development of these tools will take several years it is now time to address the question of anomalous transport in alternative magnetic confinement systems by starting to study related drift waves.

To serve this interest we have developed the first global gyrokinetic code EUTERPE [17,18], aimed at the investigation of linear drift wave stability in general toroidal equilibria with nested magnetic surfaces. Indeed, it should be noted that all the above mentioned works reduce a full 3D problem to a one-dimensional problem where the potential is computed only along one magnetic field line. With such a local model each magnetic field line is independent, the coupling between magnetic surfaces and the coupling between magnetic field lines along a given magnetic surface are neglected. In other words, this model does not treat perpendicular propagation fully adequately. Also as pointed out by Kendl [15], finding the most unstable mode with such a model is very expensive, because a large number of magnetic field lines need to be taken into account in order to cover completely the configuration. Only with a global approach can such a problem be solved in a straightforward and transparent way.

Villard [19] was the first to develop a global linear gyrokinetic code for a non-tokamak configuration. He adapted the 2D axisymmetric GYGLES code [20] to a 2D helically symmetric geometry. He identified a new class of ITG driven modes, the so-called "Helical-ITG" mode which is driven by the drift induced by the helical geometry. Hatzky [21] has also modified the GYGLES code, and has adapted it to a 2D-reduced model of the W7-X stellarator, a bumpy configuration which is characterized by a poloidal symmetry. Both new versions of GYGLES gave us a better understanding of drift waves in non-tokamak geometry, furthermore the helical version of GYGLES allowed us to validate the 3D features of the EUTERPE code [18].

The basic properties of drift waves have defined the physical model used during this work. The plasma is modeled by gyrokinetic ions and adiabatic electrons, and we follow

the linear time evolution of quasi-neutral electrostatic perturbations of the local Maxwellian distribution function in a 3D magnetic configuration. With such a model, there is no physics induced by the electrons, we particularly miss the important destabilizing effects related to the electrons trapped in the local magnetic mirrors resulting from the inhomogeneity of the magnetic field [22]. However, in a first approach we will use this simple model because the computational cost of a full kinetic description of electrons in a 3D configuration nowadays is too expensive.

We present here the first global gyrokinetic linear study of ITG driven modes for two realistic 3D configurations, namely the Quasi-Axially symmetric Stellarator with three fields periods (QAS3) [23] and HSX. Both are 3D configurations characterized by a quasi-symmetric magnetic field. In both configurations, we have investigated the effects of the 3D shape on the linear stability of the ITG driven mode. We have then developed a sequence of configurations which vary from the quasi-symmetric systems to the corresponding symmetric ones. The magnetic geometries were provided by the MHD equilibrium code VMEC [24].

This paper is organized as follows : In section II, the physical model is presented and the effects of a 3D magnetic field on the ITG driven mode are presented in section III. In section IV, the main numerical features of the EUTERPE code are briefly described, more details are given inf refs. [17,20,18], we only present here more precisely the mapping procedure between the EUTERPE code and the VMEC code in appendix A. The results are given in section V, followed by the conclusions in section VI.

II. PHYSICAL MODEL

For a 3D static equilibrium with nested magnetic surfaces, i.e. the magnetic fluxes are only function of the normalized radial variable s, the equilibrium magnetic field $\vec{B}$ can be written in contravariant form as follows [24] :

$$\vec{B} = \vec{\nabla}\varphi \times \vec{\nabla}\chi(s) + \vec{\nabla}\Phi(s) \times \vec{\nabla}\theta^*, \tag{1}$$

where $2\pi\chi(s)$ and $2\pi\Phi(s)$ are respectively the poloidal and toroidal fluxes enclosed between the magnetic axis ($s = 0$ where $\vec{\nabla}\chi = 0$) and the magnetic surface labeled s. φ is the geometric toroidal angle and θ^* the poloidal angle which makes the magnetic field lines straight. In such an equilibrium, the magnetic field lines are wound round the magnetic surfaces and their direction is given by $\vec{h} = \vec{B}/B$, where B is the amplitude of the magnetic field. We can define the normalized radial variable s as :

$$s = \Phi/\Phi_0, \tag{2}$$

where $2\pi\Phi_0$ is the value of the toroidal flux at the edge of the plasma (at $s = 1$). The coordinates (s, θ^*, φ) define the PEST-1 system of magnetic coordinates [25].

By definition in the PEST-1 coordinates, the rotational transform ι which measures the helical twist of the magnetic field lines, $2\pi\iota$ is the poloidal angle traversed by a magnetic field line after one toroidal transit, is given by :

$$\iota(s) \equiv \frac{1}{q} \equiv \frac{d\chi/ds}{d\Phi/ds} = \frac{\vec{B}\cdot\vec{\nabla}\theta^*}{\vec{B}\cdot\vec{\nabla}\varphi}, \tag{3}$$

where q is the so-called safety factor. The magnetic shear $\hat{s}$,

$$\hat{s} = \frac{s}{q}\frac{dq}{ds}, \tag{4}$$

measures the variation of the safety factor from magnetic surfaces to magnetic surfaces.

We assume a collisionless neutral static plasma where the equilibrium ion density n_0 is equal to the electron density, T_i and T_e are the equilibrium ion and electron temperatures, respectively, and the thermal velocity of the ions is given by $v_{thi} = \sqrt{T_i/m_i}$ where m_i is the ion mass. The ion cyclotron frequency is given by $\Omega = q_i B/m_i$, where q_i is the ion charge. In such a plasma, particles are freely streaming along the magnetic field lines and we assume that the plasma is homogeneous along the magnetic field lines, i.e. $\vec{B}\cdot\vec{\nabla}T_{\{i,e\}} = 0$ and $\vec{B}\cdot\vec{\nabla}n_0 = 0$.

Within the gyrokinetic model and neglecting pressure effects, the equations for the particle guiding centers are given by [26,20,27] :

$$\frac{d\vec{R}}{dt} = v_{||}\vec{h} + \frac{v_{||}^2 + v_\perp^2/2}{\Omega}\vec{h} \times \frac{\vec{\nabla}B}{B}, \tag{5}$$

$$\frac{dv_{||}}{dt} = \frac{1}{2}v_\perp^2 \vec{\nabla} \cdot \vec{h}, \tag{6}$$

$$\frac{d\mu}{dt} = 0, \tag{7}$$

where $\vec{R}$, $v_{||}$ and μ denote the position, the parallel component of the velocity of the guiding center and the first adiabatic invariant $\mu = v_\perp^2/2B$, respectively. Here, $v_\perp$ is the perpendicular component of the velocity. The position $\vec{R}$ of the guiding center is related to the particle position $\vec{x}$ by : $\vec{x} = \vec{R} + \vec{v} \times \vec{h}/\Omega$. The first term on the right-hand side of eq. (5) describes the motion of the guiding center along the magnetic field lines, the second one is the drift velocity, $\vec{v}_d$, caused by the inhomogeneity of the magnetic field and the curvature of the magnetic field lines. The gyrokinetic ordering [26] implies $v_d/v_{thi} \approx O(\epsilon_B = \rho/L_B)$, where ρ is the ion Larmor radius and L_B is the scale length of the magnetic variation, $L_B = B/|\vec{\nabla}B|$.

The perturbed part f of the ion distribution function evolves linearly according to :

$$\begin{aligned}\frac{d}{dt}f(\vec{R}, v_{||}, \mu, t) = &-\frac{\langle\vec{E}\rangle \times \vec{B}}{B^2}\frac{\partial f_0}{\partial \vec{R}} - \frac{q_i}{m_i}\vec{h} \cdot \langle\vec{E}\rangle\frac{\partial f_0}{\partial v_{||}} \\ &- \left(v_{||}\frac{\partial f_0}{\partial v_{||}} + \frac{1}{2}v_\perp\frac{\partial f_0}{\partial v_\perp}\right)\langle\vec{E}\rangle \cdot \vec{h} \times \frac{\vec{\nabla}B}{B^2},\end{aligned} \tag{8}$$

where $\langle\vec{E}\rangle$ denotes the gyro-averaged electric field.

The perturbed ion density n_i is then given by :

$$n_i(\vec{x}, t) = \int \left[f(\vec{R}, v_{||}, \mu, t) + \frac{q_i}{m_i v_\perp}\tilde{\phi}\frac{\partial f_0}{\partial v_\perp}\right]\delta^3(\vec{R} - \vec{x} + \vec{\rho})Bd\vec{R}d\alpha dv_{||}d\mu. \tag{9}$$

Here, α is the gyro-angle and we have $\tilde{\phi} = \phi - \langle\phi\rangle$, where $\langle\phi\rangle$ is the gyroaveraged potential :

$$\langle\phi\rangle(\vec{R}, v_{||}, \mu, t) = \frac{1}{2\pi}\int_0^{2\pi} d\alpha\phi(\vec{x}, t)(\vec{R} - \vec{x} + \vec{\rho}). \tag{10}$$

Note that the gyro-averaged electric field in eq. (8) is given by $\langle\vec{E}\rangle = -\vec{\nabla}\langle\phi\rangle$.

In the limit $(k_\perp\rho)^2 \ll 1$, the perturbed ion density n_i becomes [20]:

$$n_i(\vec{x}, t) = \int f(\vec{R}, v_{||}, \mu, t)\delta^3(\vec{R} - \vec{x} + \vec{\rho})Bd\vec{R}d\alpha dv_{||}d\mu + \vec{\nabla}_\perp \cdot \left[\frac{n_0}{B\Omega}\vec{\nabla}_\perp\phi\right]. \tag{11}$$

Nevertheless, even when $(k_\perp \rho) \leq 1$, Fivaz and Brunner have shown that this approximation seems to have only little effect on the growth rate and frequency of the ITG driven mode [20,22].

Assuming the electron response to be adiabatic, the system of equations is closed invoking quasi-neutrality and the Poisson equation reads :

$$\frac{en_0}{T_e}\phi - \vec{\nabla}_\perp \cdot \left[\frac{n_0}{B\Omega}\vec{\nabla}_\perp \phi\right] = \int f(\vec{R}, v_{||}, v_\perp, t)\delta^3(\vec{R} - \vec{x} + \vec{\rho})Bd\vec{R}d\alpha dv_{||}d\mu. \tag{12}$$

The equations governing the ions (5-8) and the above Poisson equation (12) coupled with equation (10) constitute the final system of equations of our model.

In contrast with axisymmetric configurations, in a 3D geometry the equations of motion of the guiding centers do not conserve an additional integral of motion, like the toroidal canonical angular momentum in a tokamak [20]. Here, the equilibrium ion distribution function f_0 must be chosen following other criteria. Using the conditions $\vec{B} \cdot \vec{\nabla} T_i = 0$ and $\vec{B} \cdot \vec{\nabla} n_0 = 0$, we choose f_0 as a local Maxwellian,

$$f_0(v_{||}, v_\perp, s) = \frac{n_0(s)}{(2\pi)^{3/2} v_{thi}^3(s)} \exp\left(-\frac{1}{2}\frac{v_{||}^2 + v_\perp^2}{v_{thi}^2(s)}\right). \tag{13}$$

III. EFFECTS OF A 3D MAGNETIC FIELD ON THE ITG DRIVEN MODE

In tokamaks, global results [22,20] have shown that the toroidal ITG mode is characterized by several poloidal wave numbers m centered around nq, with q the value of the safety factor where the toroidal ITG mode amplitude is peaking, the most unstable mode being characterized by $k_{||} \approx 0$. The coupling between the different poloidal wave numbers m is resulting from the spatial structure of B along a magnetic surface. In a simple geometry, a circular large aspect ratio tokamak, it is given in first approximation by [22] :

$$\frac{1}{B(r,\theta)} \approx \frac{1}{B(r)}\left(1 + \frac{r}{R_0}\cos(\theta)\right). \tag{14}$$

Particularly, the $\cos(\theta)$ term creates a $(m, m+1)$ coupling between the different poloidal components, i.e. it creates a coupling between the poloidal wavenumbers m and $m+1$.

In contrast, the slab ITG is almost entirely characterized by one poloidal wavenumber m. This mode is insensitive to the drift frequency and is then slightly affected by the magnetic structure of the geometry.

We can try to extrapolate these results obtained in a very simple 2D configuration to the 3D systems. In such systems, obviously, the modulus of the magnetic field B is a function of the 3 coordinates (s, θ^*, φ). The spectrum of B provides us information about the expected couplings in a 3D system. Considering a magnetic field $B = \sum_{m',n'} B_{m',n'}(s) \cos(m'\theta^* + n'\varphi)$, we assume that the amplitude of the $B_{m',n'}(s)$ coefficients is related to the intensity of the coupling between the (m, n) and the $(m + m', n + n')$ components of the ITG driven mode. We will denote this coupling $((m, n), (m + m', n + n'))$.

In a preliminary study [18] performed in a tokamak perturbed by a L=2 helical boundary deformation with $N_{per} = 4$ numbers of field periods [28], we have been able to validate this assumption. In this configuration, the spectrum of B is dominated by the $B_{1,0}$, $B_{2,2N_{per}}$ and $B_{1,2N_{per}}$ Fourier coefficients, the $B_{1,0}$ coefficient is characteristic of a tokamak. We then obtained a 3D ITG driven mode characterized by several toroidal modes numbers satisfying $\mathrm{mod}(n - n', 2N_{per}) = 0$. However, it should be noted that the coupling resulting from the helical deformation was weak compared to the coupling induced by the toroidal effects, i.e. the effects of the $B_{1,0}$ Fourier harmonic. The amplitude of the couplings $((m, n), (m+m', n+n'))$ are not directly proportional to the amplitudes of the $B_{m',n'}(s)$ coefficients.

IV. NUMERICAL IMPLEMENTATION

With the current computational resources, the linearized 3D gyrokinetic equations (5-8,10,12) have to be solved numerically using an improved version of the PIC method, the so-called δf method [29,30,20,27]. Nowadays it is the less expensive scheme in comparison with other ones which require to mesh all the phase space. At $t = 0$, the particle weights are initialized randomly and the positions and velocities are chosen according to the equilibrium density and temperature profiles.

The 3D gyrokinetic Poisson equation (12) is solved using finite elements [31]. However, as the ITG driven modes are characterized by $k_{||}/k_{\perp} \ll 1$, we want to use a system of coordinates for the electrostatic potential where this condition $\vec{h} \cdot \vec{\nabla}\phi \approx 0$ will be easily expressed. Hence, a magnetic system of coordinates seems to be the most natural choice for the representation of electrostatic potential ϕ. Furthermore, with such coordinates the grid is aligned with the magnetic surfaces and the convergence to the solution is then significantly increased [20]. However, the differential operators are diverging near the magnetic axis. With the finite element method, these singularities are usually well handled, but the integration of the equations of motion in such coordinates is cumbersome near the magnetic axis.

To avoid such difficulties, we express the particle position and velocity in the toroidal system of coordinates (R, φ, Z). Furthermore, the computation of the gyroaveraged potential $\langle\phi\rangle$ (eq. 10) becomes straightforward in this system of coordinates [32]. Therefore, working with two systems of coordinates, a magnetic one for the electrostatic potential ϕ and the toroidal one for the particles, we have to transform from one system to the other. This is easily done if we choose one coordinate to be the same in the two systems, because one of the equations defining the transformation of coordinates becomes trivial. Practically, the 3D transformation is reduced to a 2D problem. We then choose the PEST-1 system of coordinates (s, θ^*, φ) [25] for the representation of the electrostatic potential ϕ. Details of the mapping procedure between the toroidal and the PEST-1 coordinates are given in appendix A.

We can further take advantage of the interchange nature of the ITG driven modes by implementing the extraction of the ballooning phase factor [20]. In a 3D configuration, the global ITG driven mode is characterized by several poloidal and toroidal wavenumbers. However, the condition $k_{||} \approx 0$ implies that the dominant poloidal wavenumber m_0 is related to the dominant toroidal wavenumber n_0 by $m_0 \approx -n_0 q$. Following [20], we can rewrite the electrostatic potential as :

$$\phi(s, \theta^*, \varphi, t) = Re\left(\tilde{\phi}(s, \theta^*, \varphi, t) e^{iS(\theta^*, \varphi)}\right), \tag{15}$$

where $\tilde{\phi}$ is the extracted potential and S the ballooning phase factor is given by :

$$S(\theta^*, \varphi) = m_0\theta^* + n_0\varphi. \tag{16}$$

Here, m_0 and n_0 are integer numbers which are both input parameters of the code, the ballooning phase S and the extracted electrostatic potential $\tilde{\phi}$ are then periodic functions of θ^* and φ. Usually, we choose $m_0 \approx -n_0 q(s_0)$, with $q(s_0)$ the safety factor at $s = s_0$ where the ion temperature gradient peaks. As we solve only the slow spatial variation $\tilde{\phi}$ of the potential, the total number of grid points and particles is almost independent of the poloidal and toroidal wavenumbers m_0 and n_0. Hence, even for large values of m_0 and n_0 simulations remain accessible.

Lastly, the right-hand side of the discretized Poisson equation (eq. 11) is Fourier filtered in the poloidal and toroidal directions [20,27]. Generally, we only keep the poloidal and toroidal harmonics characterized by low values of $k_{||}$ and, as we have seen in sec. III, the harmonics resulting from the coupling induced by the magnetic field, the shape and width of the Fourier filter being a function of the configuration. The filter is then an important parameter of our simulations because it will govern the physics induced in our configurations.

V. RESULTS

We present here the results obtained by EUTERPE in both realistic configurations, QAS3 and HSX. Note that during all our studies, the pressure effects are neglected, $\beta = 0$, the equilibrium ion density n_0 and the electron temperature $T_e(s) = T_i(s_0)$ are constant. The equilibrium ion density n_0 is constant and we choose the equilibrium ion temperature T_i :

$$\frac{1}{T_i}\frac{dT_i}{ds_\chi} = -\kappa_T \cosh^{-2}\left(\frac{s_\chi - s_{\chi 0}}{\Delta s_\chi}\right), \tag{17}$$

where s_χ is a normalized radial variable defined with the poloidal flux $s_\chi = \sqrt{\chi/\chi_0}$, χ_0 is the value of the poloidal flux at the edge of the plasma. With the help of eqs (2) and (3),

s_χ is related to s by :

$$s_\chi^2(s) = \frac{1}{\chi_0}\int_0^s ds'\iota(s'),$$

with $\chi_0 = \int_0^1 ds'\iota(s')$.

The results presented here were obtained with 8×10^6 particles and 64 grid points on each direction (s, θ^*, φ). One run requires $\approx$ 25 cpu-hours with 64 processors of a CRAY T3E and $\approx$ 35 cpu-hours with 32 processors on a ORIGIN 2000. With the current throughput of these computers, such a run then requires $\approx$ 5 days on the T3E and $\approx$ 3 days on the ORIGIN.

We first investigate the global linear stability of the ITG driven mode in the realistic QAS3 configuration [23]. This configuration, shown in fig 1, is one of the possible candidates for the compact hybrid configuration experiment presently developed at the Princeton Plasma Physics Laboratory [6]. Note that in contrast with the 3D quasi-axisymmetric configurations [33] which are characterized by a magnetic field similar to those of a tokamak, i.e. a spectrum of B dominated by the $B_{1,0}$ component, the magnetic structure of QAS3 shown in Fig. 2 has also a strong $B_{0,1\times N_{per}}$ component, the so-called mirror field component. For this spectrum, we define the following filter :

$$(m_i, n_j) = (m_0 + i, n_0 - jN_{per}), i = [-6, 6], j = [-4, 4], \tag{18}$$

where (m_i, n_j) denote the toroidal and poloidal wavenumbers kept during the simulations and N_{per} is the number of field periods, $N_{per} = 3$. Figure 2 shows also that QAS3 has negative shear $\hat{s}$, the safety factor being then a decreasing function of s. We choose an ion temperature gradient peaking at $s_0 = 0.34$ where $q(s_0) \approx 3$, $\kappa_T = 5$, $\Delta s_\chi = 0.21$, $\hat{s}(s_0) = -0.43$ and $\rho(s_0) = 1$cm.

With the above parameters, the dispersion relation computed by EUTERPE over one period of the configuration is represented in Fig. 3. Here, the maximum growth rate is not obtained with $n = 8$ where $k_\perp\rho \approx 0.5$, but with $n = 12$. This effect is due to the negative shear of the configuration and has already been observed in tokamaks [22]. Furthermore,

Figs. 4 and 1 show that the ITG driven mode is ballooning along all the torus in the outer part of the configuration, the so-called region of unfavorable curvature. In this region, the amplitude of the magnetic field is only slightly varying along the toroidal direction. Here, the coupling resulting from the $B_{0,1\times N_{per}}$ Fourier harmonic is weak compared with the coupling induced by the toroidal effects, i.e. the effects of the $B_{1,0}$ Fourier harmonic. Therefore, as shown in fig 5, this mode is almost characterized by only one toroidal wavenumber as in a tokamak. We have also verified that the most unstable mode $n = 12$ was not affected by trapped particles. In our case, the modes obtained with and without the mirror term (eq. 6) in the equations of motion are identical, the frequency and the growth rate are not affected by trapped ions.

In QAS3, the properties of the ITG driven mode seem then to be very similar to those obtained in a tokamak. These results agree qualitatively with the local linear kinetic results obtained by Rewoldt [16].

To validate this feature of QAS3, we develop a sequence of configurations obtained by linearly varying the nonaxisymmetric Fourier coefficients of the surface of the plasma [36] :

$$\begin{aligned} R_T(s=1) = & \sum_{m',n'=0} R_{m',n'}(s=1)\cos(m'\theta - N_{per}n'v) + \\ & T\sum_{m',n'\neq 0} R_{m',n'}(s=1)\cos(m'\theta - N_{per}n'v) \\ Z_T(s=1) = & \sum_{m',n'=0} Z_{m',n'}(s=1)\sin(m'\theta - N_{per}n'v) + \\ & T\sum_{m',n'\neq 0} Z_{m',n'}(s=1)\sin(m'\theta - N_{per}n'v) \end{aligned}$$

where $R_{m',n'}(s=1)$ and $Z_{m',n'}(s=1)$ are the Fourier coefficients describing the edge of QAS3, T is a scalar. When $T = 0$, we obtain a pure axisymmetric configuration, the so-called equivalent tokamak. For all the configurations, we fix the safety factor profile (Fig. 2) and we almost keep the same number of Larmor radii along the s-axis by adjusting the value of the ion temperature at $s = s_0$.

The dispersion relation measured in the equivalent tokamak is also represented in Fig. 3, the frequencies and growth rates are very close to the values measured in QAS3. In Figure

6, the frequencies and growth rates of the modes $n = 8$ and $n = 12$ are plotted as a function of $T = (0., 0.25, 0.5, 0.75, 1)$. It shows that for both modes the frequency and growth rate are only slightly affected by the variation of the shape of the plasma. Here again, as shown in Fig. 7, the ITG driven mode $n = 8$ is ballooning around the torus in the outer part of all the configurations. The main properties of the ITG driven mode in QAS3 are governed by the global magnetic shear $\hat{s}$ of the configuration.

However, our global results contradict the ballooning model which predicts a strong influence of the local magnetic shear [34,35] on the stability of drift waves in stellarators [15], a feature which is also known from global MHD stability [36]. In figure 8 we show the very pronounced distribution of the local shear in the QAS3 configuration. Not much of this structure can, however, be detected in the wave field of the ITG driven mode, Fig. 9, in contrast to MHD global instability. Furthermore, as already mentioned, the frequency and growth rate do almost not depend on T and hence neither on the local shear.

The HSX device shown in Fig. 10 is a helical axis stellarator with 4 field periods with quasi-helical symmetry. The spectrum of the magnetic field in HSX is dominated by the $B_{1,1\times N_{per}}$ Fourier coefficient, $B \approx B(s, \theta^* - N_{per}\varphi)$. The rotational transform is mainly provided by the helical magnetic field and is rather flat, $q(s = 1)/q(s = 0) \approx 0.95$.

The ion temperature gradient peaks in the middle of the configuration, at $s_0 = 0.25$ where $q(s_0) = 0.96$ and $\rho(s_0) = 0.21\text{cm} \approx \langle a \rangle/71$, where $\langle a \rangle$ is the averaged minor radius of the configuration. We choose $\Delta s_\chi = 0.21$ and $\kappa_T = 5$.

Due to the strong helical symmetry of the magnetic field, we keep only the following poloidal and toroidal wavenumbers :

$$(m_i, n_j) = (m_0 + i, n_0 - iN_{per}), i = [-6, 6].$$

Figure 11 shows the mode $(m_0, n_0) = (-9, 8)$ obtained by EUTERPE with these parameters over one period of the configuration. In contrast with QAS3, the structure of the ITG driven mode is here characterized by a strong toroidal variation $|\max(\phi(\varphi = \pi/N_{per}))|/|\max(\phi(\varphi = 0))| \approx 1.5$. This property of the mode does not seem to be related to the magnetic structure

of HSX and neither to the trapped ion effects. Indeed, we obtain a similar toroidal variation of the mode by keeping only the m_0 and n_0 wavenumbers, the couplings induced by the magnetic field being then forbidden. Similarly, results are identical without the mirror term (eq. 6) in the equations of motion of the particles.

In order to understand this feature of HSX, we study the influence of the shape of the plasma by varying the configuration from a quasi-helically to a helically symmetric system. This transformation is achieved by increasing the number of field periods N, while the aspect ratio per period is kept constant [37]. The Fourier components of the plasma surface of the final helically symmetric configuration are such that :

$$Z^f_{m,m-1} = R^f_{m,m-1},$$
$$Z^f_{m,m+1} = -R^f_{m,m+1}.$$

Here, we choose the following transformation :

$$R_{m,n} = \frac{R^f_{m,n} - R^{HSX}_{m,n}}{N^f_{per} - N^{HSX}_{per}} \left(N - N^{HSX}_{per}\right) + R^f_{m,n},$$
$$Z_{m,n} = \frac{Z^f_{m,n} - Z^{HSX}_{m,n}}{N^f_{per} - N^{HSX}_{per}} \left(N - N^{HSX}_{per}\right) + Z^f_{m,n},$$
$$R_{0,0}/N = R^{HSX}_{0,0}/N^{HSX}_{per},$$

where $N^f_{per} = 100$ is the number of field periods of the final configuration and the superscript ^{HSX} denotes the parameters describing the plasma surface of the HSX configuration. However, the q profiles vary during the transformation, we then have to adjust the values of n_0 to keep $k_{||}$ constant from a configuration to another one.

Figures 12 and 13 show the shape on the ITG driven modes with $N = 35$ and $N = 100$. Note that we obtain a helical-ITG mode when $N = 100$. The growth rate is almost constant while the frequency is an increasing function of N. Here again, these results were obtained by keeping the same number of Larmor radii between $s = 0$ and $s = 1$. In Figs. 14 and 15, we plot the modulus of the extracted potential $\tilde{\phi}$ along the magnetic surface s_0 and compare its shape with those of the amplitude of the magnetic field and the Jacobian $\sqrt{g}^*$. When

$N = 100$, the helical symmetry of the configuration is very well preserved by the EUTERPE code, the modulus of $\tilde{\phi}$ is very well aligned with the amplitude of the magnetic field and the Jacobian. With HSX, the effects of the helical symmetry of the configuration are also well shown. But the toroidal variation of $\tilde{\phi}$ does not seem to be correlated with the shape of B. However, it reaches its maximum (the central spot around $\varphi = \pi/4$ and $\theta^* = \pi$) where $\sqrt{g}^*$ is minimum. We represent the values of the Jacobian and B along the same magnetic surface in Fig. 16. The structure of the ITG driven mode results from the combined effects of $\sqrt{g}^*$ which is strongly varying along the toroidal direction and the almost helical magnetic field. With $N = 35$, we can observe the transition between the quasi-helical and helical systems. Here the mode is still strongly helical, but its shape is also affected by the difference of structure between the Jacobian and the amplitude of the magnetic field.

HSX being characterized by a helical magnetic axis, the structure of the Jacobian results from the variation of the position of the magnetic axis along the toroidal direction. As shown in Fig. 11, the poloidal plane is centered around $R = 1.45$m at $\varphi = 0$ whereas it is centered around $R = 1.05m$ at $\varphi = \pi/N_{per}$. The curvature drifts are then stronger at the middle of the period. However, the effects of this feature of HSX on the frequency and growth rate of the ITG driven mode are not clearly established and require further simulations.

VI. CONCLUSIONS

We have investigated the linear stability properties of the ITG driven modes in two different 3D configurations with the help of the 3D global gyrokinetic code EUTERPE. Our model based on gyrokinetic ions and adiabatic electrons has revealed an interesting feature of the electrostatic ITG instability. In the QAS3 configuration, results do not show a strong effect resulting from the 3D geometry on the growth rate, the frequency and the shape of the ITG driven mode. Here, the ITG driven mode is ballooning in the outer part of the torus where the amplitude of the magnetic field is almost constant along the toroidal direction. The results are then similar to those of a tokamak. Furthermore, in contrast with ballooning

predictions, the influence of the local shear on ITG instability is weak whereas of global shear is strong. This is largely because of the nature of the global ITG driven mode which is characterized by a long parallel wavelength and $k_\perp \rho = O(1)$. Furthermore the gradient of temperature lies in the perpendicular plane to the magnetic field. Therefore, the resulting global ITG driven modes are more sensitive to the variation of B in the perpendicular plane than along the magnetic field lines. On the other hand, HSX which is not dominated by toroidal effects has shown a clear and new 3D effect related to the 3D shape of the plasma, i.e. the variation of the centrifugal force along the magnetic field lines. However, here again, this effect on the growth rate of the ITG driven mode has turned out to be weak. Further simulations are required to validate this point.

However, the physical model needs to be improved by including a non adiabatic response of the electrons [38,22], because with our current model we miss all the important destabilizing effects due to trapped electrons. Furthermore, we should include the effects of an equilibrium radial electric field [39] which, in tokamaks, has been shown to have a strong stabilizing influence on the ITG driven mode.

Acknowledgment: This work was partly supported by the Swiss National Science Foundation. The computations have been performed on the CRAY T3E of the Joint Computing Center of the Max Planck Gesellschaft and the IPP in Garching and the Origin 2000 of the Ecole Polytechnique Fédérale de Lausanne.

APPENDIX A: MAPPING FROM TOROIDAL TO VMEC COORDINATES

The equilibrium magnetic field (1) and all other magnetic quantities required by the gyrokinetic equations are provided by the 3D equilibrium code VMEC [24]. They are computed in the (s, u, v) system of coordinates, where s is given by eq. (2), $v \equiv \varphi$ is the geometric toroidal angle and u the poloidal variable is related to θ^* by [40] :

$$\theta^* = u + \lambda(s, u, v), \tag{A1}$$

where λ is a periodic function of u and v with zero average over a magnetic surface.

The position of a guiding center (R, φ, Z) is expressed in the VMEC coordinates (s, u, v) as

$$R = \sum_{m,n} R_{m,n}(s) \cos(mu - nLv), \tag{A2}$$

$$\varphi = v, \tag{A3}$$

$$Z = \sum_{m,n} Z_{m,n}(s) \sin(mu - nLv), \tag{A4}$$

with L the number of field periods of the configuration. The number of Fourier harmonics m and n are both input parameters of VMEC.

The VMEC code computes the $R_{m,n}(s)$ and $Z_{m,n}(s)$ Fourier harmonics on a finite number of magnetic surfaces $s_i, i = 1..N_s$, the $R_{m,n}(s)$ and $Z_{m,n}(s)$ are only discrete functions of s. It computes also the N_s $\lambda_{m,n}$ Fourier harmonics, the λ function being given by :

$$\lambda(s, u, v) = \sum_{m,n} \lambda_{m,n}(s) \sin(mu - nLv). \tag{A5}$$

As particles are pushed in (R, φ, Z), we thus need to invert the system of three equations (A2-A4). We pre-compute all these required quantities and store them on each point of a (R, φ, Z) grid which encloses the plasma. Hence, using linear interpolation, we can easily and efficiently compute all the equilibrium quantities needed by the gyrokinetic equations.

Let us denote (R_g, φ_g, Z_g) the coordinates of the grid point where we want to compute the VMEC quantities required by the EUTERPE code. We want to find the (s_g, u_g, v_g) coordinates such that $(R_g, \varphi_g, Z_g) = \Xi(s_g, u_g, v_g)$, where Ξ is the 3D nonlinear function constituted by the equations (A2-A4).

We proceed as follows : we first define a equidistant mesh in θ, the geometric poloidal angle, of N_θ grid points :

$$\theta_k = (k-1)\frac{2\pi}{N_\theta - 1}; k = 1..N_\theta, \tag{A6}$$

and a 2D mesh (s_i, θ_k); $i = 1..N_s, k = 1..N_\theta$ of $N_s \times N_\theta$ points. In the poloidal plane $\varphi_g \equiv v_g = const$, with the help of eqs. (A2-A4), we compute the position of the $N_s \times N_\theta$ grid points, denoted $\{R_{i,k}, Z_{i,k}\}$:

$$R_{i,k} = \sum_{m,n} R_{m,n}(s_i)\cos(mu_{i,k} - nLv_g), \tag{A7}$$

$$Z_{i,k} = \sum_{m,n} Z_{m,n}(s_i)\sin(mu_{i,k} - nLv_g), \tag{A8}$$

where $u_{i,k}$ is such that

$$\xi(u_{i,k}) = \theta_k - \tan^{-1}\left(\frac{Z_{i,k} - Z_{axis}(v_g)}{R_{i,k} - R_{axis}(v_g)}\right) = 0. \tag{A9}$$

In other words, for a given magnetic surface s_i and a given value of θ_k, we have to compute the root of the function ξ defined above. We then have to invert the eqs. (A2-A4). Here, however, we have reduced the 3D problem into a 1D problem, the function ξ is only a function of u. The root is computed using the Newton-Raphson method [41], we choose θ_k as initial guess. We now rewrite eqs (A7-A8) as :

$$R_{i,k} = R_{axis}(v_g) + \tilde{\rho}(s_i, \theta_k, v_g)\cos(\theta_k), \tag{A10}$$

$$Z_{i,k} = Z_{axis}(v_g) + \tilde{\rho}(s_i, \theta_k, v_g)\sin(\theta_k), \tag{A11}$$

where $\tilde{\rho}(s_i, \theta_k, v_g)$ is computed for all the $N_s \times N_\theta$ points and is simply given by :

$$\tilde{\rho}(s_i, \theta_k, v_g) = \sqrt{(R_{i,k} - R_{axis}(v_g))^2 + (Z_{i,k} - Z_{axis}(v_g))^2}. \tag{A12}$$

We can define a new system of coordinates $(\tilde{\rho}, \theta, v)$ and the grid point (R_g, φ_g, Z_g) can be expressed in these coordinates as :

$$R_g = R_{axis}(v_g) + \tilde{\rho}(s_g, \theta_g, v_g)\cos(\theta_g), \tag{A13}$$

$$Z_g = Z_{axis}(v_g) + \tilde{\rho}(s_g, \theta_g, v_g)\sin(\theta_g). \tag{A14}$$

Following eq. (A12), one obtains

$$\tilde{\rho}_g = \sqrt{(R_g - R_{axis}(v_g))^2 + (Z_g - Z_{axis}(v_g))^2}. \tag{A15}$$

We now want to find the four points on the grid (s_i, θ_k) surrounding (R_g, Z_g). Denoting l the poloidal index such that $\theta_l \leq \theta_g < \theta_{l+1}$, we easily find the four neighbours given by :

$$\tilde{\rho}(s_j, \theta_l, v_g) \leq \tilde{\rho}_g < \tilde{\rho}(s_{j+1}, \theta_l, v_g) \tag{A16}$$

$$\tilde{\rho}(s_j, \theta_{l+1}, v_g) \leq \tilde{\rho}_g < \tilde{\rho}(s_{j+1}, \theta_{l+1}, v_g). \tag{A17}$$

Finally, along the magnetic surfaces s_j and s_{j+1}, we compute the roots of

$$\xi(u_j) = \theta_g - \tan^{-1}\left(\frac{Z(s_j, u_g, v_g) - Z_{axis}(v_g)}{R(s_j, u_g, v_g) - R_{axis}(v_g)}\right) = 0, \tag{A18}$$

and

$$\xi(u_{j+1}) = \theta_g - \tan^{-1}\left(\frac{Z(s_{j+1}, u_g, v_g) - Z_{axis}(v_g)}{R(s_{j+1}, u_g, v_g) - R_{axis}(v_g)}\right) = 0 \tag{A19}$$

which gives us two points at (s_j, u_j) and (s_{j+1}, u_{j+1}) aligned with the grid point (R_g, φ_g, Z_g). Indeed, the three points are all characterized by $\theta = \theta_g$ and then belong to the $\theta_g = const$ line.

We compute the required values $\mathbf{F}$ at (R_g, φ_g, Z_g) using a simple linear interpolation between (s_j, u_j) and (s_{j+1}, u_{j+1}). With VMEC, however, some quantities like the harmonics of the magnetic field $B_{m,n}(s)$ are only computed at the middle of a interval $[s_i, s_{i+1}]$. We also approximate them at s_j and s_{j+1} using a linear interpolation, i.e. $B_{m,n}(s_j) = (B_{m,n}(s_{j-\frac{1}{2}}) + B_{m,n}(s_{j+\frac{1}{2}}))/2$. The final value $\mathbf{F}$ at (R_g, φ_g, Z_g) is given by :

$$\mathbf{F}(R_g, \varphi_g, Z_g) = (1 - w)\mathbf{F}(s_j, u_j, v_g) + w\mathbf{F}(s_{j+1}, u_{j+1}, v_g) \tag{A20}$$

with

$$w = \frac{\tilde{\rho}_g - \tilde{\rho}(s_j, \theta_g, v_g)}{\tilde{\rho}(s_{j+1}, \theta_g, v_g) - \tilde{\rho}(s_j, \theta_g, v_g)}.$$

We can easily test the accuracy of the procedure by taking $\mathbf{F} = R$ (eq. A2) and compare this value with R_g. With $N_s = 97$ and $N_\theta = 128$, the relative error, $(\mathbf{F} - R_g)/R_g$, is less than 1%. Note that we compute s_g using the above equation.With this algorithm, computations are performed only on the N_s discrete magnetic surfaces s_i computed by VMEC. It is an important feature, because the computations of the roots of the ξ function are generally only possible on the discrete magnetic surfaces s_i. Interpolations along s are then only performed at the end of the process. Furthermore, the $(\tilde{\rho}, \theta, \varphi)$ system of coordinates being

a polar system of coordinates centered around the magnetic axis, we also avoid the problem encountered around the magnetic axis by the direct resolution described above.

If the grid point (R_g, φ_g, Z_g) is outside the plasma, the relations (A16) and (A17) are not verified. We then linearly extrapolate the required values $\mathbf{F}$ from the two last discrete magnetic surfaces s_{N_s-1} and s_{N_s}.

We do not store the PEST-1 poloidal variable θ^* on the (R, φ, Z) grid. With this system of coordinates, a linear interpolation would give wrong results at the magnetic axis (θ^* is not unique) and around the line $\theta^* = 0$, i.e. where θ^* goes from 2π to 0. With the help of eqs. (A9) and (A1), we easily compute the value of θ^* on the points of the (s_i, θ_k) grid. For every poloidal plane, we then store these values of θ^*. Hence, in EUTERPE, when we need to compute the PEST-1 poloidal coordinate of a particle θ_p^*, we compute first the value of s_p using the (R, φ, Z) grid. Then, still using linear interpolation, we compute the corresponding θ_p^* with the help of this (s, θ, φ) grid.

This algorithm has proven to be relatively robust even with realistic configurations like QAS3 or HSX. Generally, we choose a (R, φ, Z) grid of $100 \times 65 \times 100$ points. If the VMEC equilibrium is well converged, the number of points where it fails is smaller than 10. Usually, they are located near the edge of the configuration. With such refractory points, we compute the required magnetic quantities using a bilinear interpolation on the $(R, \varphi = const, Z)$ mesh.

REFERENCES

[1] F. Romanelli, Phys. Fluids B **1** (1989) 1018.

[2] M. Kotschenreuter, G. Rewoldt and W. M. Tang, Comp. Phys. Comm. **88** (1995) 128.

[3] S. Ichimaru, in *Basic Principles of Plasma Physics* (Benjamin/Cummings 1973).

[4] J. Nührenberg and R. Zille, Phys. Lett. A., **129**, (1988) 113.

[5] F. S. B. Anderson *et al.*, Trans. Fusion Tech., **27**, (1995) 273.

[6] D. A. Monticello *et al.*, in *Proc. 25th EPS Conf. on Controlled Fusion and Plasma Physics, Prague, 1998* p185.

[7] S. Gori, W Lotz and J. Nührenberg, in *Theory of fusion plasmas, Int. Workshop, Varenna, August 1996* (Editrice Compositori, Società Italiana di Fisica, Bologna, 1997) p 335.

[8] J. Nührenberg *et al.*, Trans. Fusion Tech. **27**, 71 (1995).

[9] M. Kick *et al.*, Plasma Phys. Control. Fusion **41**, (1999) A549.

[10] A. Bhattacharjee *et al.*, Phys. Fluids **26**, (1983) 880.

[11] N. Dominguez, B.A. Carreras and V.E. Lynch, Phys. Fluids B **4**, (1992) 2894.

[12] R.E. Waltz and A.H. Boozer, Phys. Fluids B **5**, (1993) 2201.

[13] M. Persson, J.L.V. Lewandowski and H. Nordman, Phys. Plasmas **3**, (1996) 3720.

[14] J.L.V. Lewandowski, Phys. Plasmas **4**, (1997) 4023.

[15] A. Kendl and H. Wobig, Phys. Plasmas **6**, (1999) 4714.

[16] G. Rewoldt, L. P. Ku, W. M. Tang and W. A. Cooper, Phys. Plasmas **6**, (1999) 4705.

[17] G . Jost *et al.*, in *Theory of fusion plasmas, Int. Workshop, Varenna, September 1998* (Editrice Compositori, Società Italiana di Fisica, Bologna, 1999) p 419.

[18] G. Jost *et al.*, in *Proc. 26th EPS Conf. on Controlled Fusion and Plasma Physics, Maastricht, 1999* p 1093.

[19] L. Villard *et al.*, in *Theory of fusion plasmas, Int. Workshop, Varenna, September 1998* (Editrice Compositori, Società Italiana di Fisica, Bologna, 1999) p 427.

[20] M. Fivaz *et al.*, Comp. Phys. Comm. **111**, (1998) 27.

[21] R. Hatzky and M. Fivaz, in *Proc. 25th EPS Conf. on Controlled Fusion and Plasma Physics, Prague, 1998* p 203.

[22] S. Brunner, Ph. D. Thesis **1701**, Ecole Polytechnique Fédérale de Lasaunne, (1997).

[23] P. Garabedian and L. P. Ku, Phys. Plasmas **6**, 645 (1999).

[24] S. P. Hirshman and D. K. Lee, Comp. Phys. Comm. **39**, (1986) 161.

[25] R. C. Grimm, J. M. Greene, and J. L. Johnson, Methods in Comp. Phys. **16**, (1976) 253.

[26] T.S. Hahm, Phys. Fluids **31**, (1988) 2670.

[27] T.M. Tran *et al.*, in *Theory of fusion plasmas, Int. Workshop, Varenna, September 1998* (Editrice Compositori, Società Italiana di Fisica, Bologna, 1999) p 45.

[28] A. Ardelea and W. A. Cooper, Phys. Plasmas **4**, 3482 (1997).

[29] A. M. Dimits and W. W. Lee, Journal of Comp. Phys. **107**, 309 (1993).

[30] S. E. Parker and W. W. Lee, Phys. Fluids B **5**, 77 (1993).

[31] G. Strang and G. J. Fix, in *An Analysis of the Finite Element Method* (Prentice-Hall, Englewood Cliffs, N.J. 1973).

[32] W. W. Lee, Journal of Comp. Phys. **72**, 243 (1987).

[33] J. Nührenberg, W. Lotz and S. Gori, in *Theory of fusion plasmas, Int. Workshop,*

Varenna, August 1994 (Editrice Compositori, Società Italiana di Fisica, Bologna, 1995) p 3.

[34] J. M. Greene and J. L. Johnson, Phys. Plasmas **10**, 729 (1968).

[35] J. M. Greene and M. S. Chance, Nucl. Fusion **21**, 453 (1981).

[36] W. A. Cooper, *Stability of a compact 3-period stellarator with quasiaxial symmetry features*, to be published in Phys. Plasmas, (2000).

[37] J. Nührenberg and R. Zille in *Theory of fusion plasmas, Int. Workshop, Varenna, August 1992* (Editrice Compositori, Società Italiana di Fisica, Bologna, 1993) p 17.

[38] B. B. Kadomtsev and O. P. Pogutse, Nucl Fus. **11**, (1971) 67.

[39] M. Maccio, J. Vaclavik and L. Villard, in *Theory of fusion plasmas, Int. Workshop, Varenna, September 1998* (Editrice Compositori, Società Italiana di Fisica, Bologna, 1999) p 511.

[40] S. P. Hirshman and J. C. Whitson, Phys. Fluids **26**, 3553 (1983).

[41] W. H. Press, S. A. Teukolsky, W. T. Vetterling and B. P. Flannery, in *Numerical Recipes* (Cambridge University Press, New York, 1986).

FIGURE CAPTIONS

Fig.1 Contour of the electrostatic potential over one period of QAS3. We show here the mode $m_0 = -24, n_0 = 8$ at $s = s_0$. Some magnetic surfaces intersections with poloidal planes (dashed lines) and some magnetic field lines (continuous lines) are also represented.

Fig.2 Amplitude of the largest Fourier harmonics $B_{m',n'}$ as a function of s ($B_{0,0}$ is omitted) for QAS3 (left) and the safety factor q and the logarithmic derivative of the ion temperature profile as function of s (right).

Fig.3 Frequency and growth rate of the ITG driven mode measured in QAS3 and the equivalent tokamak ($T = 0$) as function of n_0.

Fig.4 Level surfaces of the electrostatic potential ϕ measured at $\varphi = 0, 0.33, 0.65$ and $\pi/3$ in QAS3 with $m_0 = -24$ and $n_0 = 8$.

Fig.5 Spectrum of the electrostatic potential ϕ (right) measured at $s = s_0$ for QAS3. The spectrum is centered around $(m_0, n_0) = (-24, 8)$.

Fig.6 Frequency and growth rate of the ITG driven modes $n_0 = 12$ and $n_0 = 8$ measured as function of T.

Fig.7 Level surfaces of the electrostatic potential ϕ measured at $\varphi = 0$ (top) and $\pi/3$ (bottom) as a function of T with $m_0 = -24$ and $n_0 = 8$.

Fig.8 Distribution of local shear in QAS3 at $s = s_0$.

Fig.9 Contour of the amplitude of the extracted potential $\tilde{\phi}$ and the local shear (continuous lines) as a function of φ (denoted v) and θ^* at $s = s_0$ for $T = 0, 0.5$ and QAS3.

Fig.10 Same as in Fig. 1, but in HSX. We show here the node $m_0 = -9, n_0 = 8$ at $s = s_0$.

Fig.11 Level surfaces of the electrostatic potential ϕ in HSX. We show the mode $m_0 = -9, n_0 = 8$ at $\varphi = 0$ (right), $\pi/2N_{per}$ (top), π/N_{per} (left) and $3\pi/2N_{per}$ (bottom).

Fig.12 Same as in Fig. 11, but with $N = 35$.

Fig.13 Same as in Fig. 11, but with $N = 100$.

Fig.14 Amplitude of the extracted potential $\tilde{\phi}$ and B (continuous lines) as a function of φ (denoted v) and θ^* measured at $s = s_0$ with $N = 4$ (HSX), $N = 35$ and $N = 100$.

Fig.15 Amplitude of the extracted potential $\tilde{\phi}$ and $\sqrt{g}^*$ (continuous lines) measured at $s = s_0$ with $N = 4$ (HSX), $N = 35$ and $N = 100$.

Fig.16 Amplitude of B and $\sqrt{g}^*$ at $s = s_0$ as a function of θ^* and φ in HSX.

FIG.1 Jost

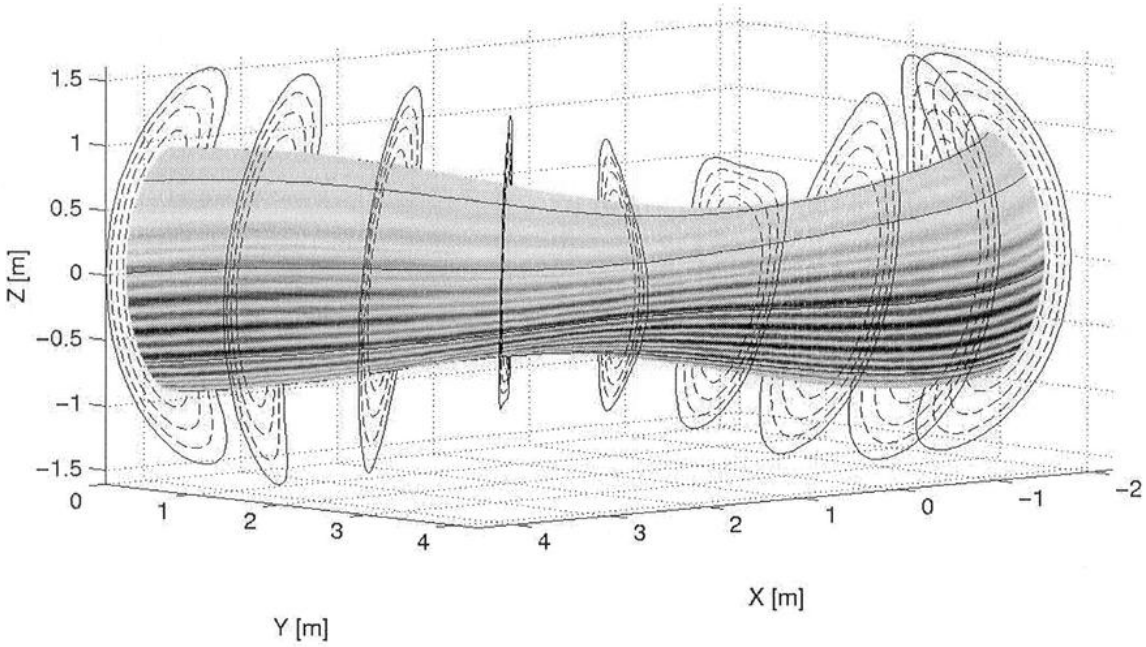

FIG.2 Jost

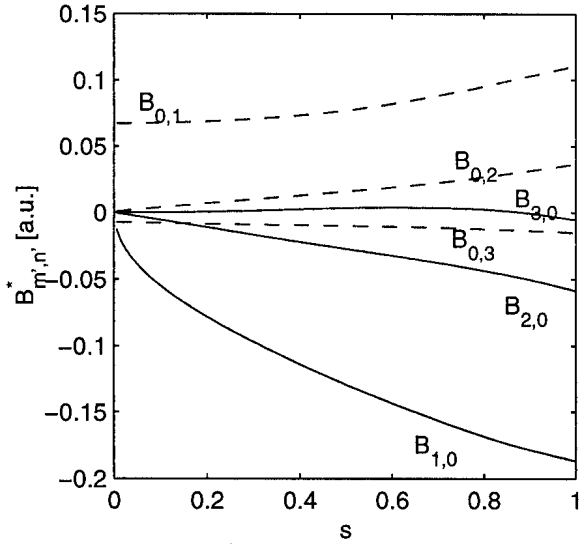
0.15
0.1
0.05
0
−0.05
−0.1
−0.15
−0.2
0
0.2
0.4
0.6
0.8
1
s
$B^*_{m',n'}$ [a.u.]
$B_{0,1}$
$B_{0,2}$
$B_{3,0}$
$B_{0,3}$
$B_{2,0}$
$B_{1,0}$

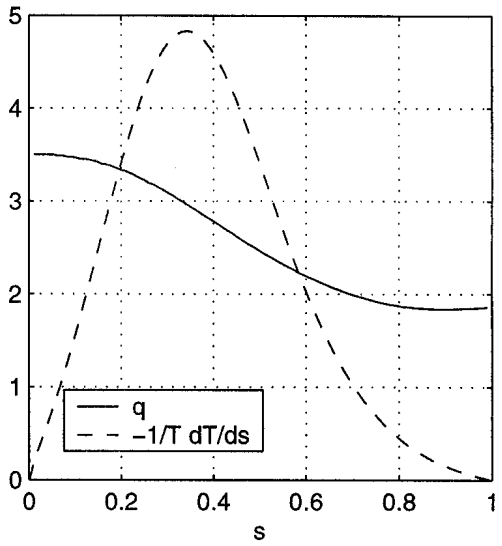
5
4
3
2
1
0
0
0.2
0.4
0.6
0.8
1
s
q
−1/T dT/ds

FIG.3 Jost

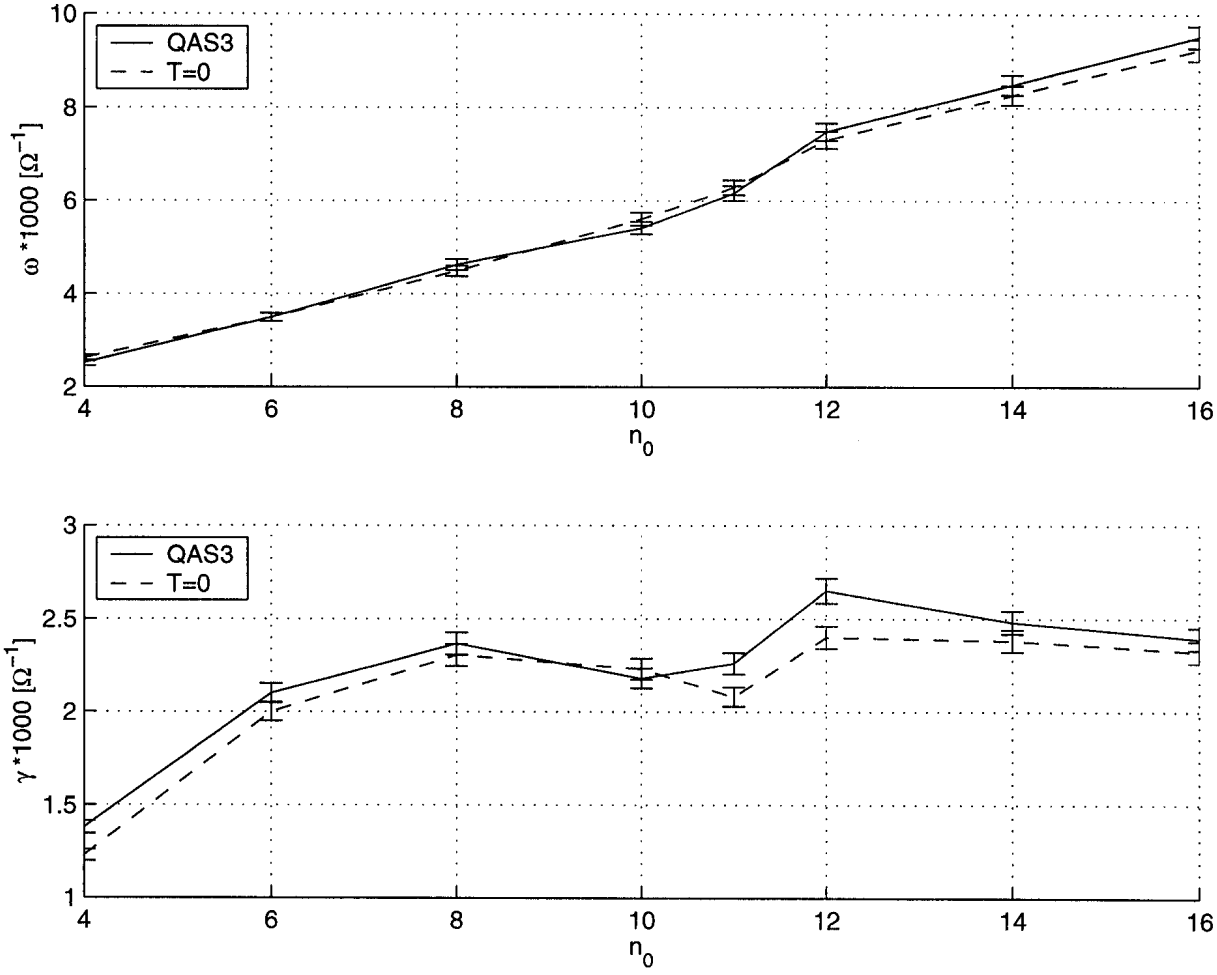

FIG.4 Jost

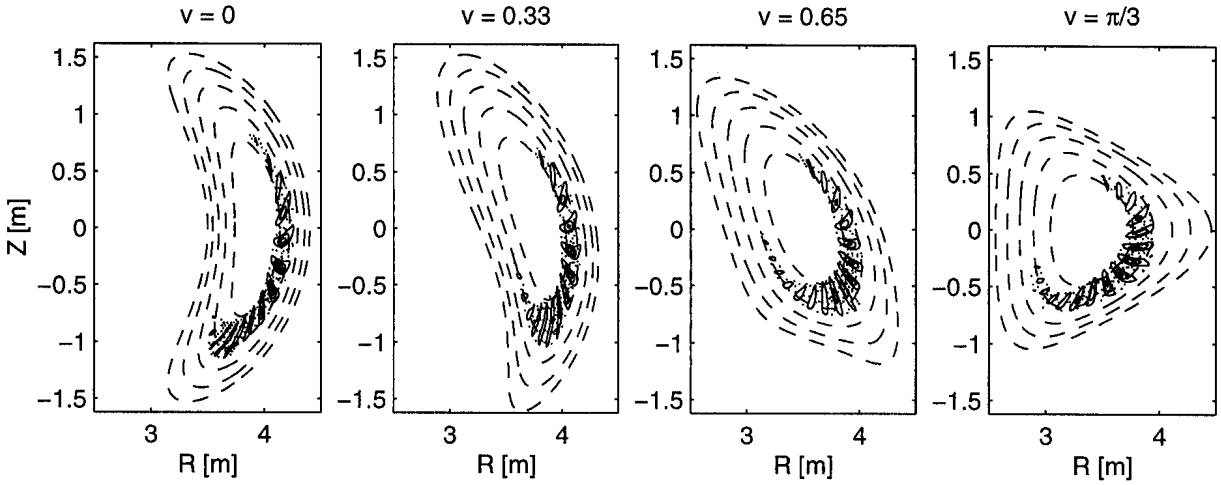

FIG.5 Jost

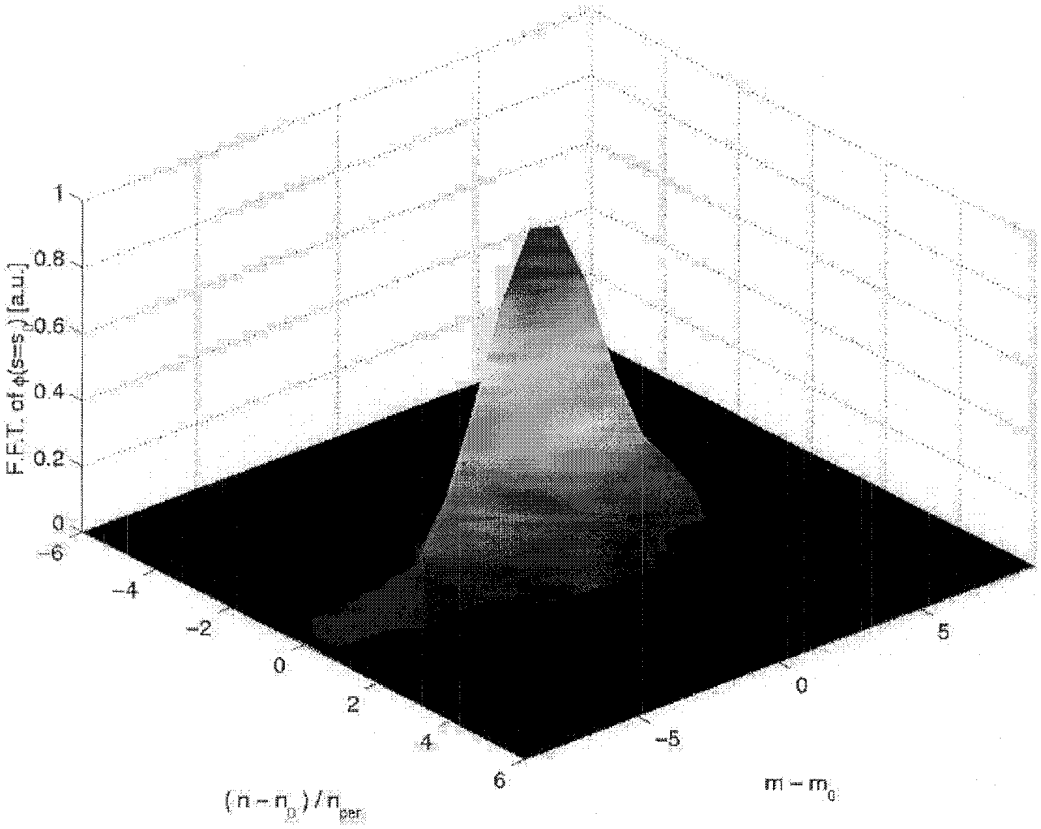

FIG.6 Jost

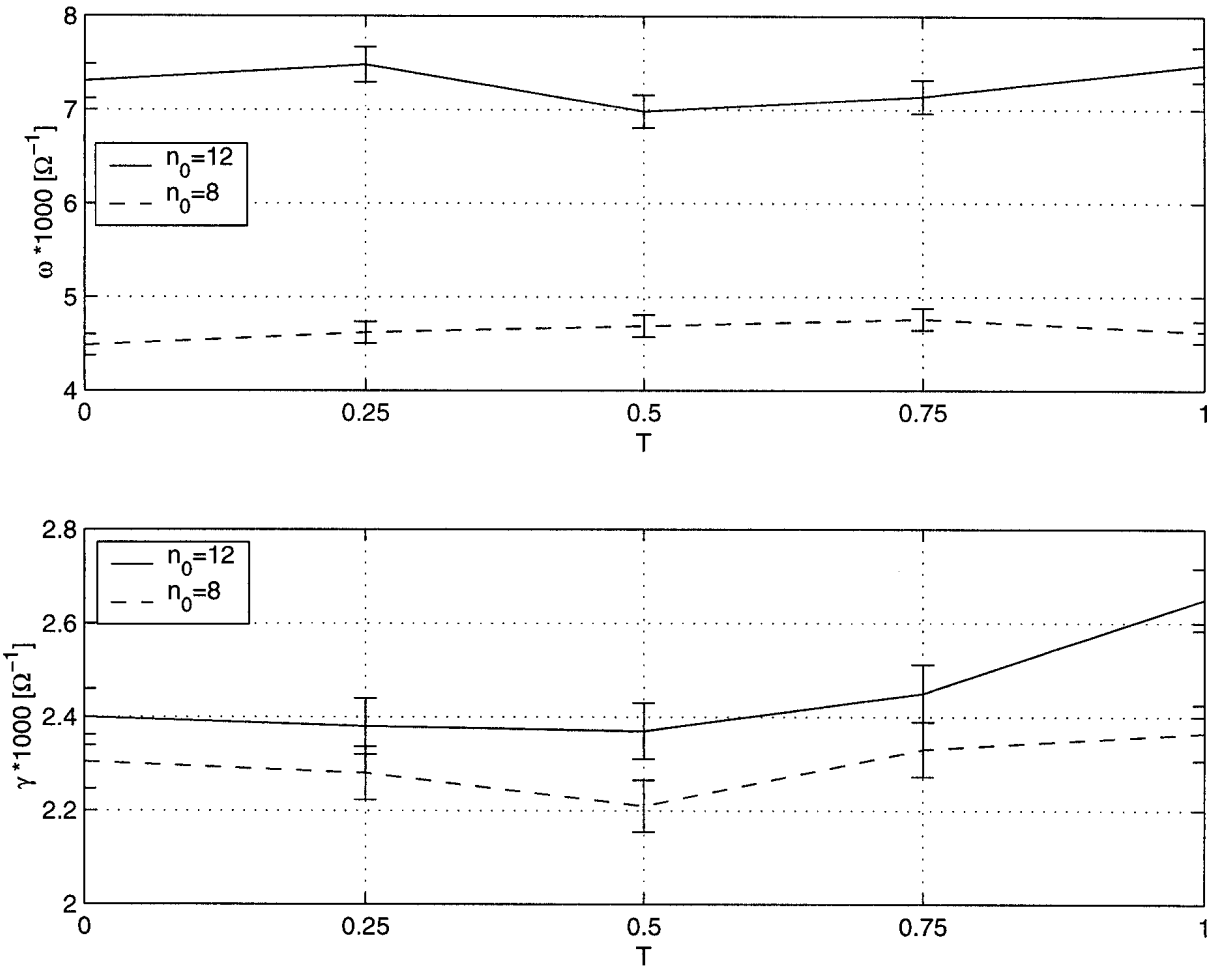
8
7
6
5
4
0
0.25
0.5
0.75
1
T
ω *1000 [Ω⁻¹]
n0=12
n0=8
2.8
2.6
2.4
2.2
2
0
0.25
0.5
0.75
1
T
γ *1000 [Ω⁻¹]
n0=12
n0=8

FIG.7 Jost

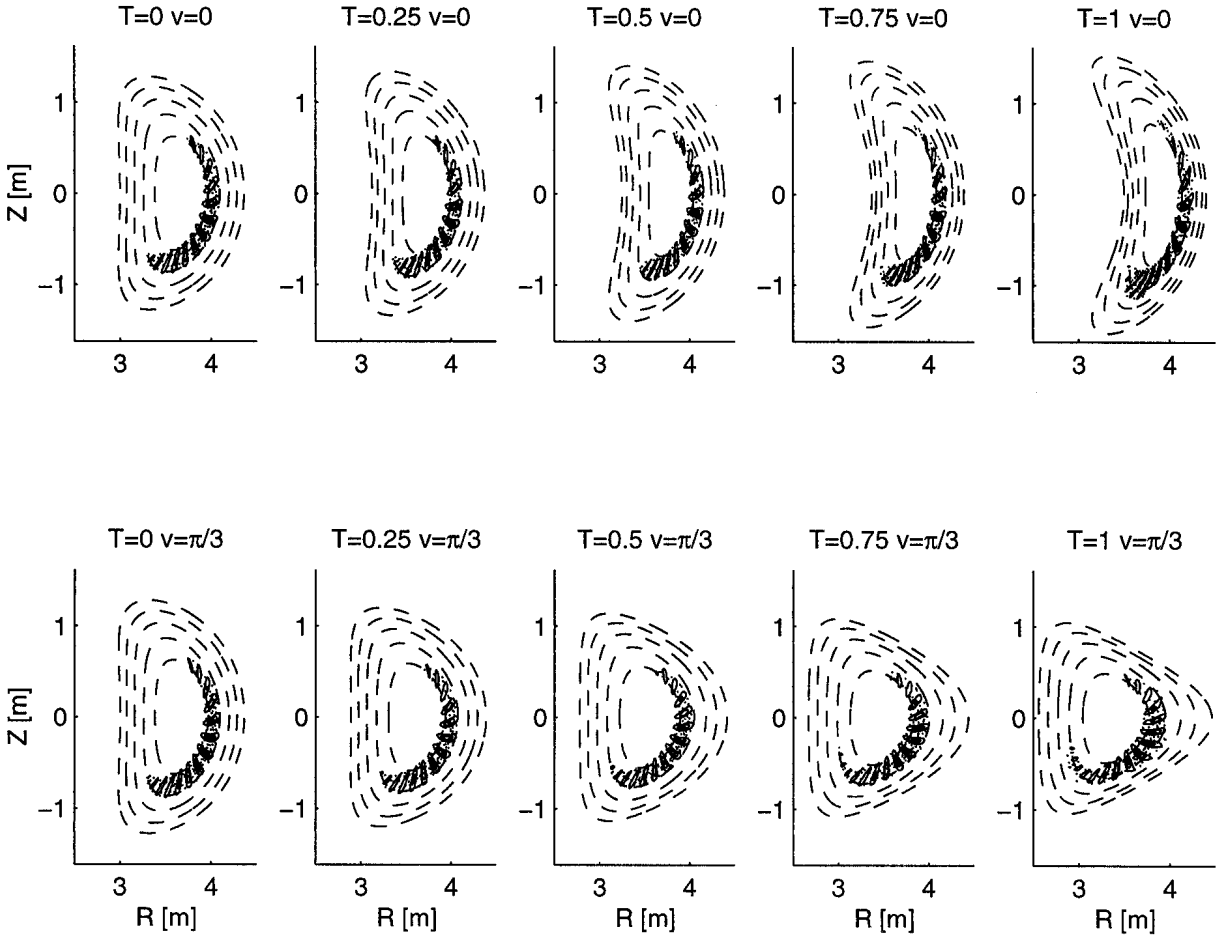
T=0 v=0
T=0.25 v=0
T=0.5 v=0
T=0.75 v=0
T=1 v=0
T=0 v=π/3
T=0.25 v=π/3
T=0.5 v=π/3
T=0.75 v=π/3
T=1 v=π/3
Z [m]
R [m]
1
0
−1
3
4

FIG.8 Jost

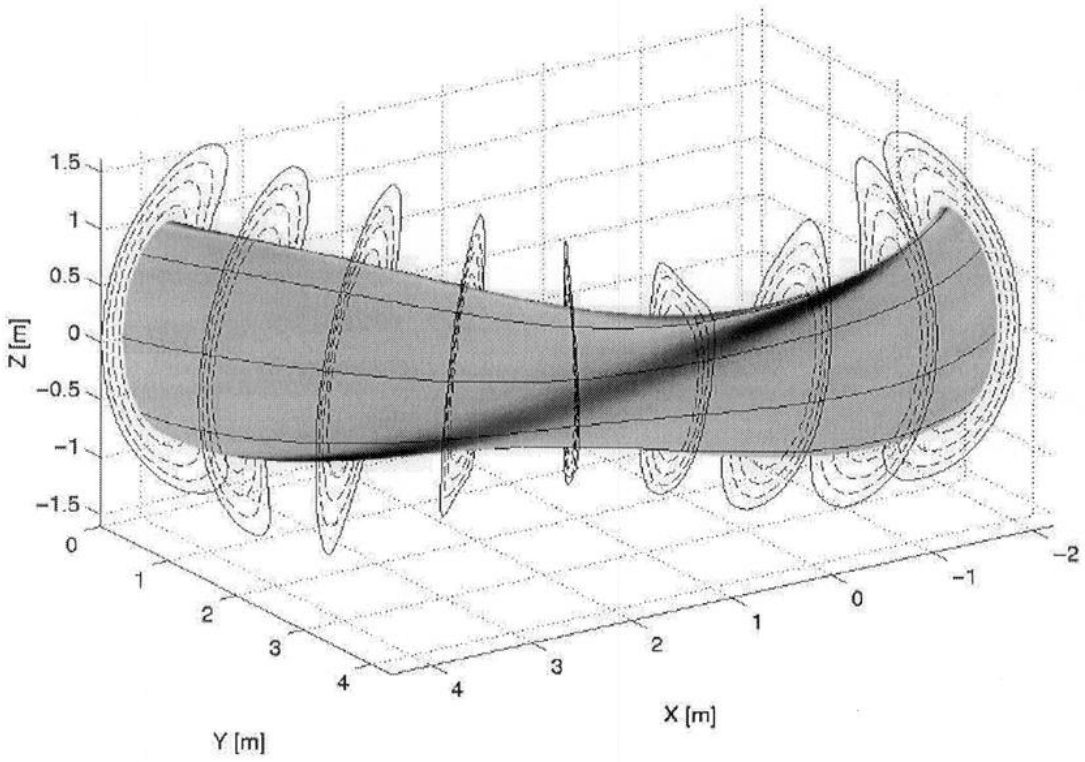

FIG.9 Jost

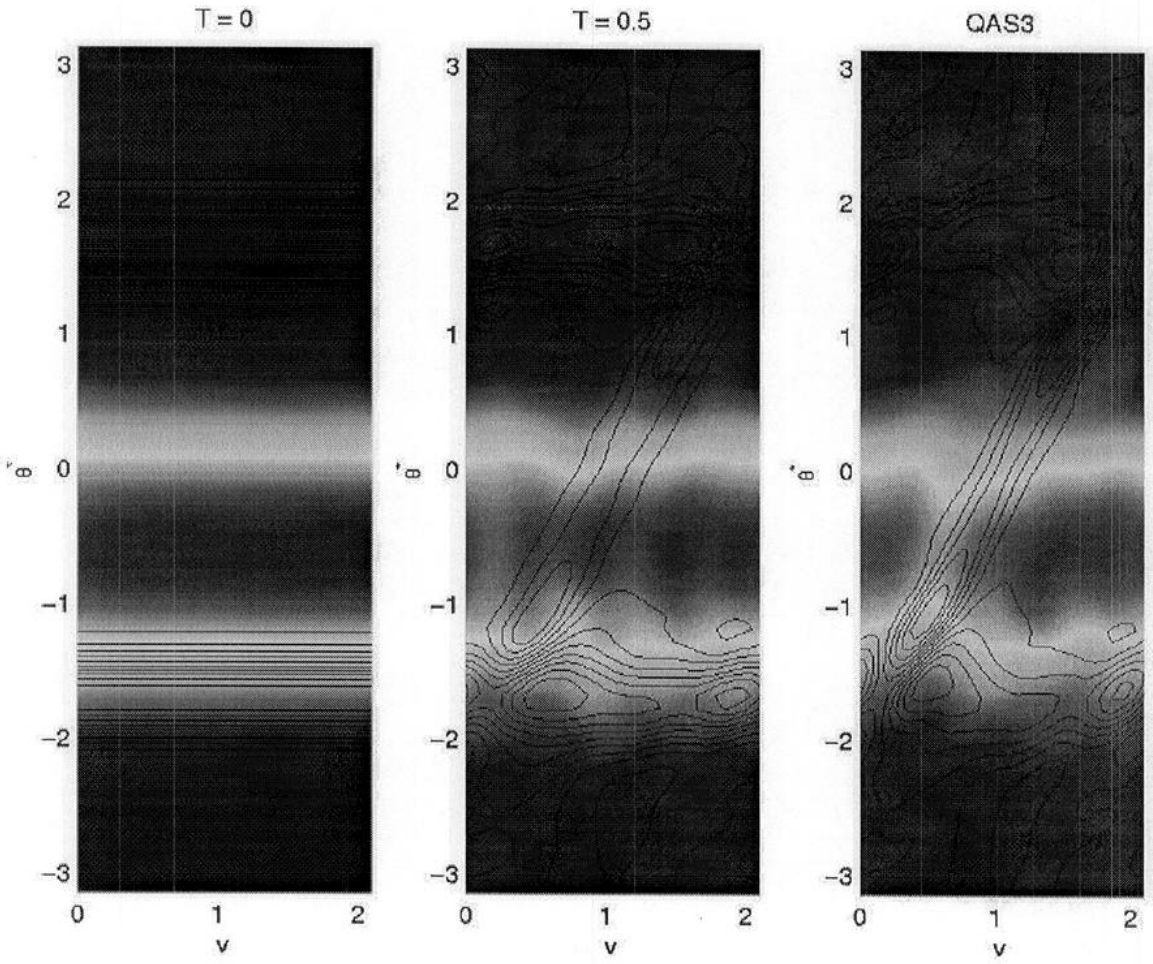

FIG.10 Jost

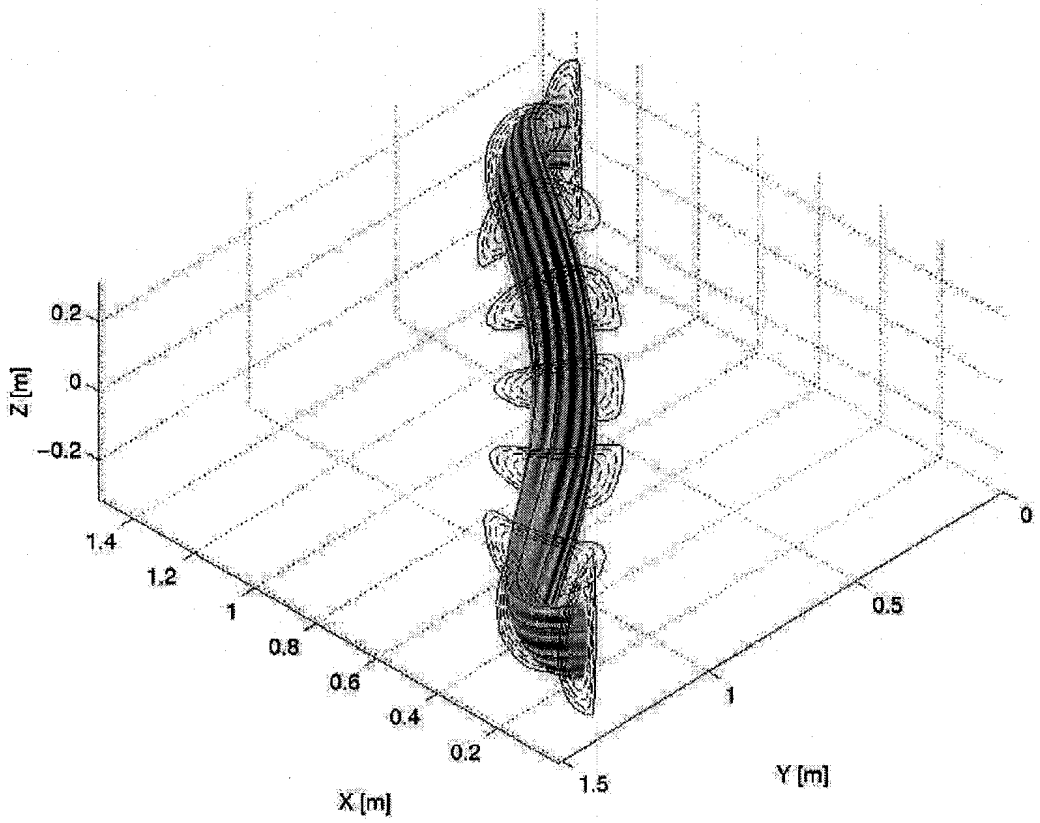

FIG.11 Jost

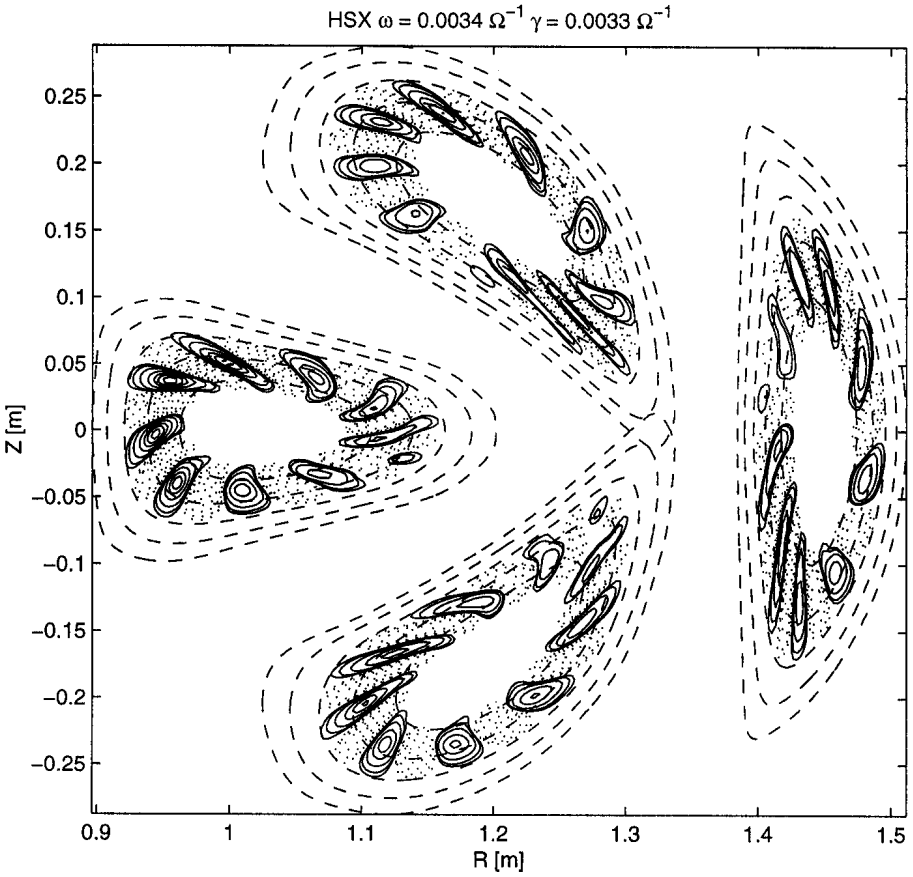
HSX ω = 0.0034 Ω^{-1} γ = 0.0033 Ω^{-1}
0.25
0.2
0.15
0.1
0.05
0
−0.05
−0.1
−0.15
−0.2
−0.25
Z [m]
0.9
1
1.1
1.2
1.3
1.4
1.5
R [m]

FIG.12 Jost

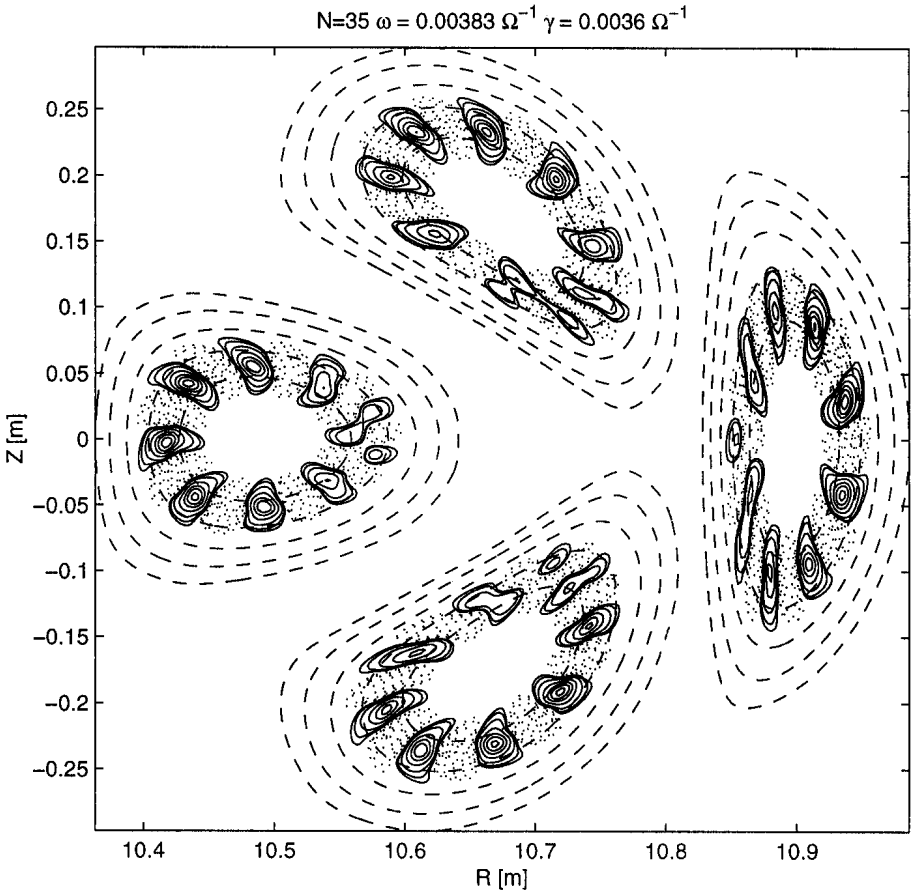
N=35 ω = 0.00383 Ω^{-1} γ = 0.0036 Ω^{-1}
0.25
0.2
0.15
0.1
0.05
0
−0.05
−0.1
−0.15
−0.2
−0.25
Z [m]
10.4
10.5
10.6
10.7
10.8
10.9
R [m]

FIG.13 Jost

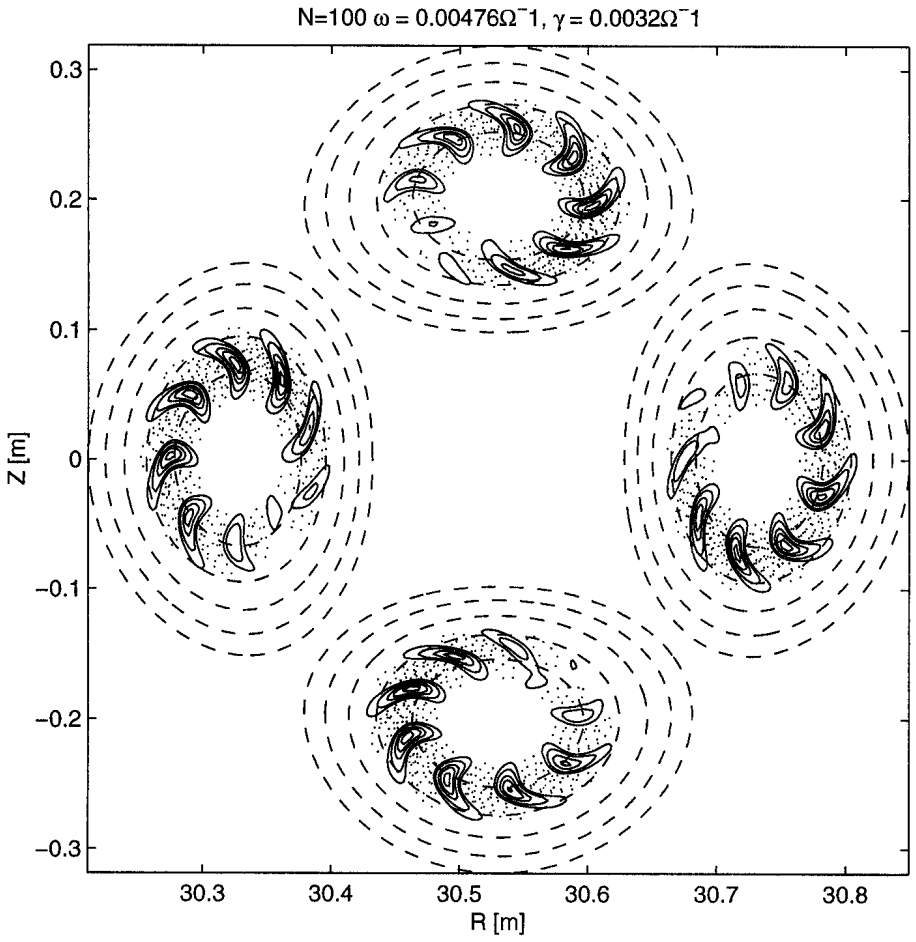
N=100 ω = 0.00476Ω¯1, γ = 0.0032Ω¯1
0.3
0.2
0.1
0
−0.1
−0.2
−0.3
Z [m]
30.3
30.4
30.5
30.6
30.7
30.8
R [m]

FIG.14 Jost

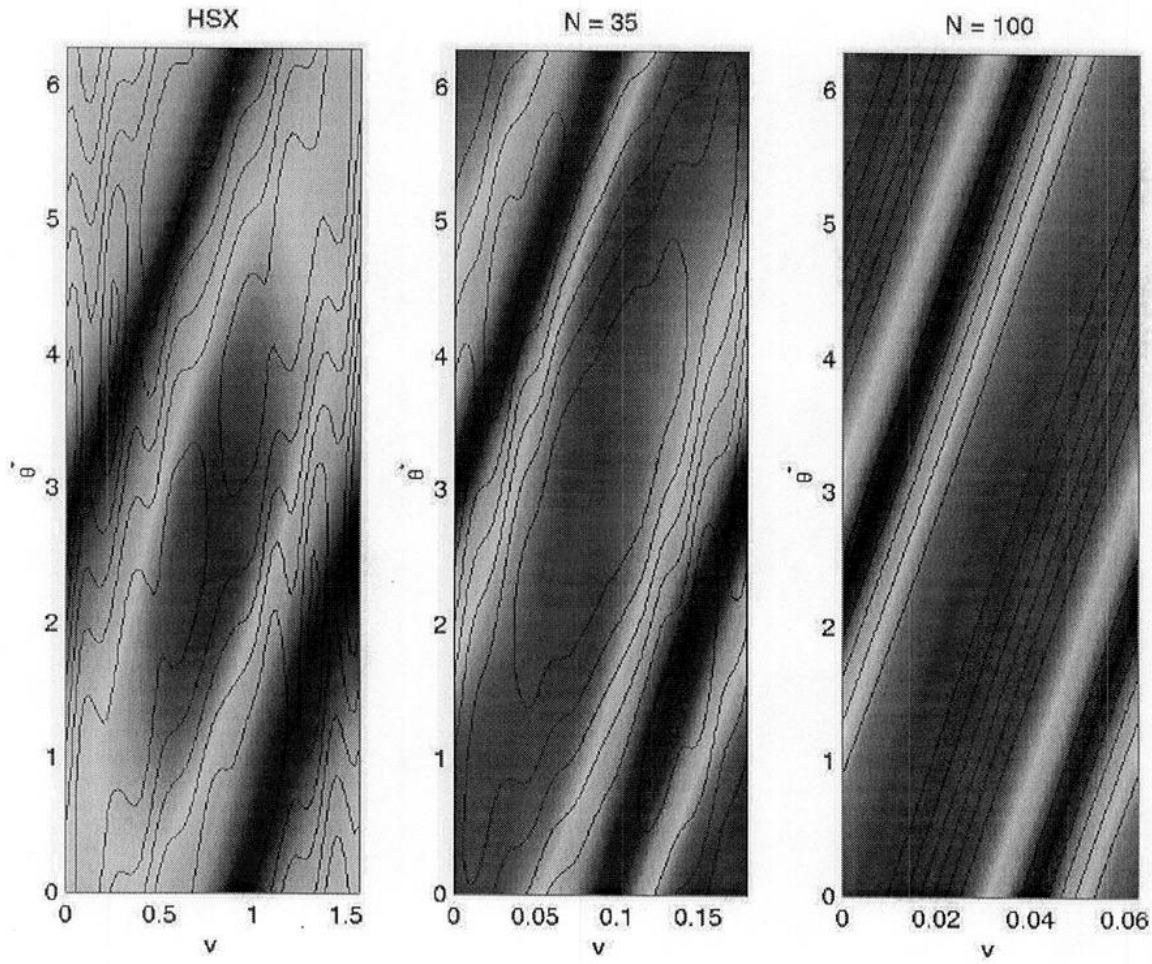

FIG.15 Jost

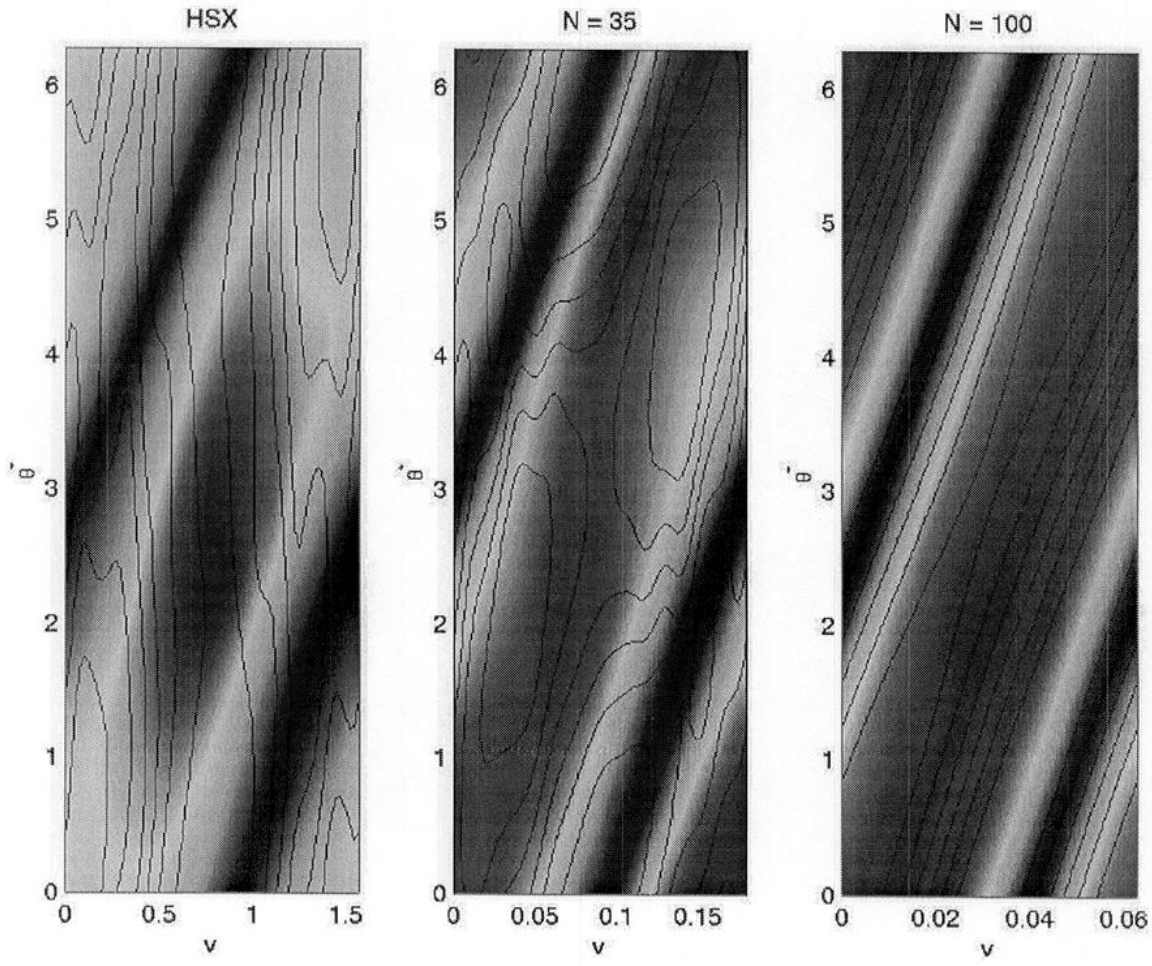

FIG.16 Jost

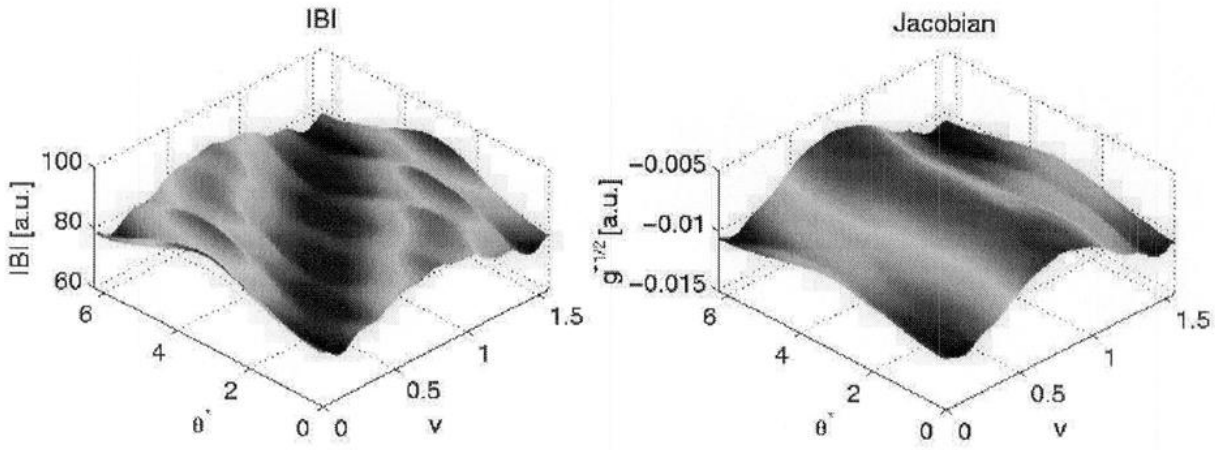
IBI
|B| [a.u.]
100
80
60
6
4
2
0
θ
0
0.5
1
1.5
v
Jacobian
g^1/2 [a.u.]
−0.005
−0.01
−0.015
6
4
2
0
θ
0
0.5
1
1.5
v